



Cite this: *Lab Chip*, 2022, 22, 3499

# Characterization of nanoparticle size distributions using a microfluidic device with integrated optical microcavities†

Kiana Malmir, <sup>a</sup> William Okell,<sup>a</sup> Aurélien A. P. Trichet<sup>b</sup> and Jason M. Smith \*<sup>ab</sup>

We introduce a method for analyzing the physical properties of nanoparticles in fluids *via* the competition between viscous drag and optical forces in a microfluidic device with integrated optical microcavities. The optical microcavity acts as a combined optical trap and sensor, such that the time duration of individual particle detection events can be used as a measure of particle size *via* a parameter which represents the dielectric polarizability per unit radius. Characterization of polymer particles with diameters as small as 140 nm is reported, below that used in previous optical sorting approaches and in the size range of interest for nanomedicine. This technique could be applied in combination with other analytic techniques to provide a detailed physical characterization of particles in solution.

Received 22nd February 2022,  
Accepted 5th August 2022

DOI: 10.1039/d2lc00180b

rsc.li/loc

## 1 Introduction

The characterization of nanoparticles in solution is of increasing importance for applications in biomedical, environmental, and materials sciences.<sup>1–5</sup> In particular, the engineering of nanoparticles for use in medical applications such as drug delivery requires accurate characterization of the physical and chemical characteristics of particles within the fluid medium. The efficient clinical drug delivery systems need to accurately control drug release. The ability of nanomedicine to reach the target organ can be determined by its particle size, and concentration. Therefore, characterizations of nanocarriers such as nanoparticles are crucial to controlling their desired effects.<sup>6</sup> For instance, investigation of the size and loading properties of lipid nanoparticle vehicles containing silencing RNA (siRNA), is of increasing importance for future studies of dynamics with single-particle resolution.<sup>7</sup>

There are a number of methods to characterize nanoparticles at the single-particle level with high resolution. Electron microscopy or scanning probe microscopy can provide accurate information on the shape of the nanoparticles.<sup>8,9</sup> For example, Atomic Force Microscopy (AFM) technique can characterize nanoparticles with the size range of 1–20 nm in dry and liquid states.<sup>10,11</sup> Although AFM

has high compatibility with different samples and measurement environments, it is limited due to the need for sample preparation. Namely, the samples need to be deposited on a hard substrate.<sup>11</sup> Methods based on light-scattering and diffusion have been also developed to characterize the suspended nanoparticles in a fluid. These techniques are the common techniques for determining the size and the shape of nanoparticles.

Particle size and size distribution are readily measured using light scattering techniques. Dynamic Light Scattering (DLS)<sup>12</sup> is fast and sensitive to particles as small as 5 nm, but provides limited resolution for polydisperse samples where larger particles dominate the scattered signal.<sup>13,14</sup> Nanoparticle Tracking Analysis (NTA) and Tunable Resistive Pulse Sensing (TRPS) provide single particle measurements of particle size allowing for more reliable measurement of size distributions.<sup>11,15–21</sup> Optical microscopy cannot measure the size of individual biological nanoparticles but combination of NTA with surface-sensitive optical imaging allows us to accurately quantify the size of biological nanoparticles attached to lipid bi-layers.<sup>22</sup> Also, particle size, shape and orientation can be determined by measuring optical cross-sections of nanoparticles in wide field extinction microscopy for different light wavelengths and excitation polarization.<sup>8</sup> Flow cytometry (FCM) is another well-established method to characterize individual cells and particles.<sup>23,24</sup> FCM is a flow-based method to detect size of polydisperse, heterogeneous, or mixed samples and concentrations by measuring the properties of scattered light or fluorescence associated with the cells.<sup>25</sup>

Beyond particle size, centrifugation techniques allow direct measurement of the mass density of particle

<sup>a</sup> Oxford University, Department of Materials, University of Oxford, Parks Road, Oxford OX1 3PH, UK. E-mail: kianamalmir@gmail.com

<sup>b</sup> Oxford HighQ Ltd, Centre for Innovation and Enterprise, Begbroke Science Park, Oxford OX5 1PF, UK

† Electronic supplementary information (ESI) available. See DOI: <https://doi.org/10.1039/d2lc00180b>



ensembles.<sup>26,27</sup> New optical techniques have recently emerged which measure the composition of individual particles *via* the dielectric polarizability, a parameter which depends on both particle volume and dielectric constant and can in some cases provide a proxy for particle mass.<sup>28</sup> Such measurements are made more challenging by the rapid Brownian motion of the particles in the bulk fluid. There exist several solutions to this problem such as using hydrodynamic forces on nanoparticles to induce their drift in the flow direction. While the movement perpendicular to the flow remains random, the size of the nanoparticles can be accurately measured by quantifying the deterministic and random components of the movement,<sup>22</sup> as well as analyzing the thermal motion of nanoparticles in an array of electrostatics traps.<sup>29</sup> Another approach is to trap the nanoparticle in an optical microcavity to allow prolonged measurement,<sup>30</sup> a technique that can provide independent measurements of size and polarizability on a particle-by-particle basis.<sup>31</sup> The use of optical gradient forces for the sorting and trapping micron-sized particles in a flowing fluid is also well-established.<sup>32–34</sup> This work builds on<sup>30,35</sup> by introducing a controlled fluid flow through the microcavity, such that the trap duration is determined by the competition between the optical forces and viscous drag. Since the optical force is proportional to the dielectric polarizability of the particle and the viscous drag force is proportional to its hydrodynamic radius, the balance between them is determined by the polarization per unit radius, a new parameter which can be combined with others to provide comprehensive characterization methodologies.

## 2 Method

The equation of motion for a spherical particle with polarizability  $\alpha$  in a viscous fluid flowing at uniform velocity  $\underline{v}_0$  and illuminated with an optical field of intensity distribution  $I(\underline{r})$  is

$$\gamma \left( \frac{d\underline{r}}{dt} - \underline{v}_0 \right) = \frac{1}{2n_m \epsilon_0 c} \alpha \nabla I(\underline{r}) + \sqrt{2K_B T} \gamma \underline{W}(t). \quad (1)$$

Here  $\gamma = 6\pi\eta a$  is the coefficient of friction where  $\eta$  is the viscosity and  $a$  is the particle radius, so that the left hand side of the equation represents the viscous drag force acting on the particle. The first term on the right hand side is the optical force in the dipole approximation where  $n_m$  is the refractive index of the surrounding medium, and the second term represents the Brownian force acting on the particle in which  $K_B T$  is the thermal energy and  $\underline{W}(t)$  is a time-varying normally distributed random vector<sup>36</sup> where  $t$  is time. Within the dipole approximation the polarizability is

$$\alpha = 4\pi a^3 n_m^2 \epsilon_0 \frac{m^2 - 1}{m^2 + 2}, \quad (2)$$

where  $m$  is the ratio of refractive index of the particle ( $n_p$ ) to that of the surrounding medium ( $n_m$ ), *i.e.*  $m = n_p/n_m$ .

It can be seen from eqn (1) and (2) that for a given optical intensity distribution  $I(\underline{r})$  and flow velocity  $\underline{v}_0$ , the balancing of the optical force with the drag force due to the flowing fluid is achieved for a threshold value,  $\beta_T$ , of the parameter

$$\beta = \frac{\alpha}{a} = a^2 \frac{m^2 - 1}{m^2 + 2}, \quad (3)$$

such that particles with  $\beta > \beta_T$  may become trapped in the optical mode.

Apparatus which allows the rate of trapping events ( $\Gamma_{\text{trap}}$ ) to be detected as a function of the flow speed or optical power can therefore be used to determine the distribution  $N(\beta)$  by differentiating the measured trapping rate with respect to  $\beta_T$ ,

$$N(\beta) = - \frac{d\Gamma_{\text{trap}}}{d\beta_T}. \quad (4)$$

The thermal motion of the particle introduces a random element to the time a particle spends in the mode for values of  $\beta$  close to the threshold and is therefore a source of broadening of the distribution function.

The geometry of our measurement apparatus is depicted in Fig. 1(a). A plano-concave microcavity generally consist of two separate mirrors facing each other where one mirror can move independently.<sup>35,37–41</sup> This type of microcavities supports a standing wave optical mode comprising five antinodes of light of wavelength  $\lambda = 640$  nm with a mode width of less than 1  $\mu\text{m}$ . The fluid flow direction is perpendicular to the optical axis. For this cavity mode,  $I(\underline{r})$  can be expressed approximately as a standing wave of a Gaussian beam with cylindrical symmetry about the axis,

$$I(\rho, z) = \frac{2P}{\pi w(z)^2} \sin^2 \left( kz + \frac{kp^2}{2R(z)} - \arctan \left( \frac{z}{z_R} \right) \right) e^{\frac{-2\rho^2}{w(z)^2}}. \quad (5)$$

where,  $\rho$  and  $z$  are the radial and axial coordinates with their origin at the beam focus which corresponds to a node of the electric field on the planar mirror.  $P$  and  $k$  are the intracavity power and optical wavenumber, respectively. The parameters  $z_R$ ,  $w(z)$  and  $R(z)$  are the parameters of the Gaussian beam that are established from the curvature of the concave mirror and the cavity length (see ESI†).

As a particle passes through the cavity mode, its presence is detected by a spectral shift in the resonance which is proportional the mode intensity at the position of the particle. The resultant signal can therefore be modelled using a Monte Carlo approach based on eqn (1) to simulate the motion of the particle through the device. We define transverse axes  $x$  and  $y$  such that  $\rho^2 = x^2 + y^2$  and select  $x$  as the direction of fluid flow. Particles are ‘launched’ starting from a position 1  $\mu\text{m}$  upstream of the cavity mode ( $x = -1$   $\mu\text{m}$ ) with selected values of position ( $y, z$ ), fluid flow rate  $v$  and optical power  $P$ . Fig. 1(b and c) show example trajectories for a particle of diameter 200 nm and with flow speed  $v = 100$   $\mu\text{m s}^{-1}$ . Fig. 1b shows an example trajectory of a particle that is not trapped by the mode at  $P = 10$  mW, while Fig. 1c shows



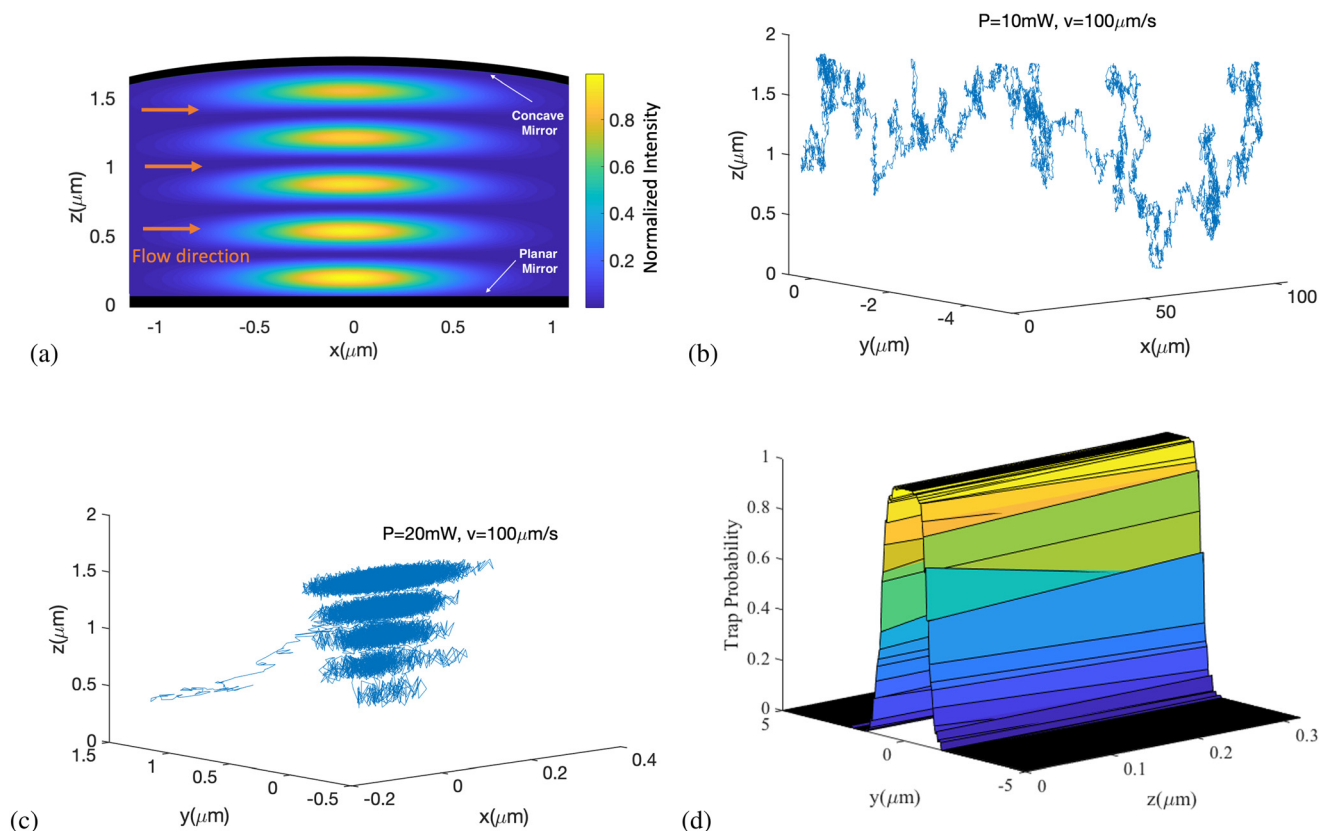


**Fig. 1** (a) False colour-scale plot of the normalized optical intensity distribution  $I(x, z)$  in an open-access microcavity with 5 optical anti-nodes between a planar and concave mirror. The intensity distribution is cylindrically symmetric about the  $z$  axis, and the fluid flow direction is parallel to  $x$ . (b and c) Example simulated trajectories of a particle of diameter 200 nm subject to the flow and optical forces described in the text. The flow speed is  $100 \mu\text{m s}^{-1}$  and the intracavity power is 10 mW and 20 mW respectively. (d) A typical trapping probability distribution as a function of the initial position of the particle in the  $(y, z)$  plane.

a similar particle being trapped when  $P$  is increased to 20 mW. To determine a trapping probability, trapping was defined to have occurred if the particle did not pass  $x = 1 \mu\text{m}$  within a time equal to  $10 \mu\text{m}$  divided by the flow speed. For a given choice of  $v$  and  $P$  the initial position  $(y, z)$  was varied and the trapping probability (based on 100 repetitions per position) was established to produce a distribution map (Fig. 1d). It was found that within the range of parameters used the trapping probability was independent of the initial  $z$  position and so the trapping cross section  $\sigma$  was defined by integrating the distribution map with respect to  $y$  only. The trapping rate  $\Gamma$  is then given by the product of the trapping cross section, the cavity length ( $L$ ), the flow speed ( $v$ ) and nanoparticle concentration per unit volume in the fluid ( $C_{\text{NP}}$ ):

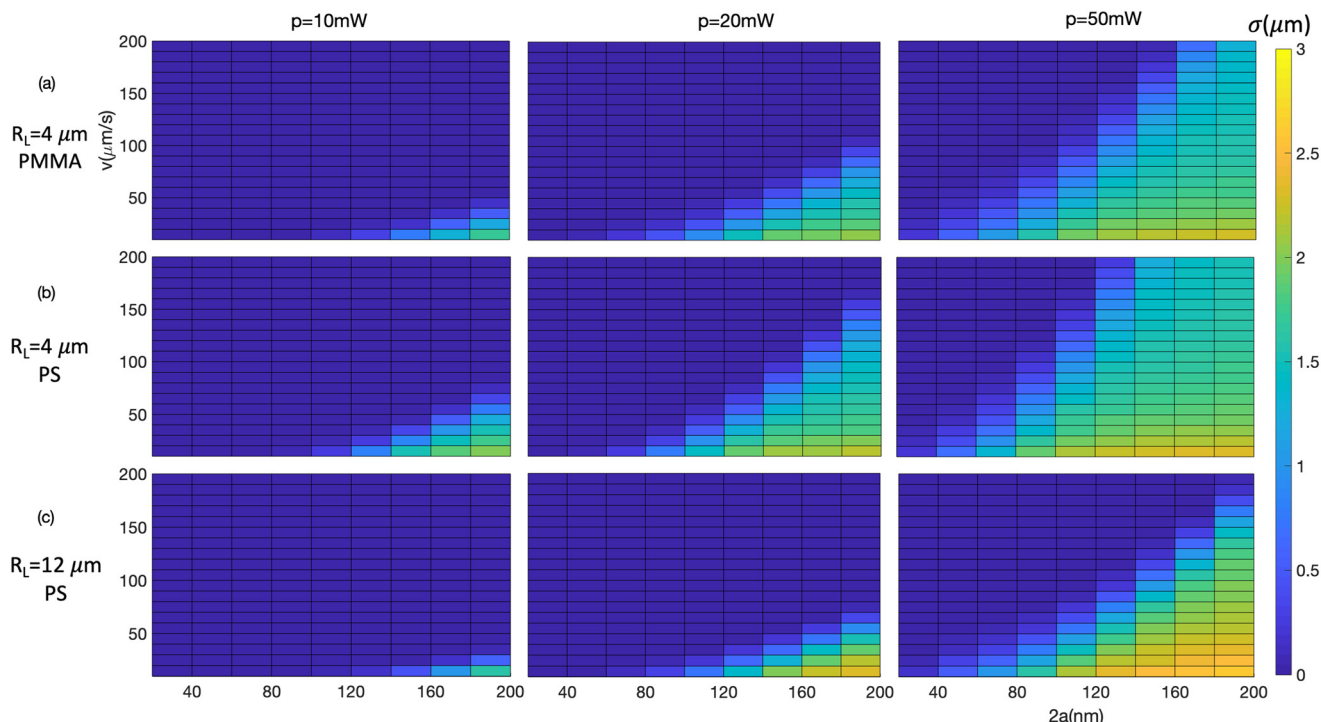
$$\Gamma = \sigma L v C_{\text{NP}} \quad (6)$$

Fig. 2 shows the simulated variation of  $\sigma$  with several experimental parameters, as a series of false colour-scale plots. Each plot shows the dependence on flow speed  $v$  and particle diameter  $2a$ ; maps are generated for optical powers of  $P = 10 \text{ mW}$ ,  $20 \text{ mW}$  and  $50 \text{ mW}$  (columns) and for two different mirror radii of curvature ( $R_L$ ) and particle

refractive index ( $n_p$ ) (rows). The general result is as expected – that small particles in a rapidly flowing fluid (upper left of maps) do not trap, while larger particles in a slow flow speed show substantial trapping cross sections of order  $2 \mu\text{m}$ . The striking feature of these maps is that in each case the boundary between the region with no trapping and the region where trapping occurs is reasonably sharp, such that at a given flow speed  $\sigma$  rises from zero to around  $1.5 \mu\text{m}$  within an increase in particle diameter of about 20 nm. It is this sharp boundary that provide a basis for using the method for quantitative measurement.

The location of this boundary within the map depends on the values of the fixed parameters  $P$ ,  $w_0$  and  $n_p$ . As expected the boundary moves to smaller particle sizes and higher flow speeds for increasing  $P$  and  $n_p$  and for decreasing  $w_0$ . Within each plot the quadratic dependence of the threshold speed on particle radius given in eqn (3) can be seen, and the sensitivity to refractive index is shown by the comparison of PS and PMMA in Fig. 2a and b. The dependence on fixed experimental parameters indicates the ability to tune the measurement to different particles. The value of  $\beta$  that balances the maximum trapping force with the flow force is found to be





**Fig. 2** Trapping cross-section ( $\sigma$ ) as a function of the diameter ( $D = 2a$ ) and the velocity ( $v$ ) of the particle in different situations such as optical beam waist or radius of curvature of the concave mirror ( $R_L$ ), and the composition or the refractive index of the particle;  $\sigma$  for (a) PMMA particles and  $R_L = 4 \mu\text{m}$  (first row), (b) PS particles and  $R_L = 4 \mu\text{m}$  (second row), and (c) PS particles and  $R_L = 12 \mu\text{m}$  (third row).

$$\beta_T = \frac{3\pi\eta v c w^3 \sqrt{e}}{2n_m P}, \quad (7)$$

which reveals the scaling of the technique sensitivity with these experimental parameters.

### 3 Experimental results

In the experiments, nanoparticle solutions of concentration  $10^{11} \text{ ml}^{-1}$  were pumped through a microfluidic flow cell with integrated microcavity measurement system. Here we used  $R_L = 12 \mu\text{m}$  and  $L = 1.5 \text{ nm}$ . A constant differential pressure of 2 mbar was established using a hydrostatic flow regulator,<sup>42</sup> resulting in a peak flow speed of  $\sim 50 \mu\text{m s}^{-1}$ . Single nanoparticles passing through the microcavity register as discrete ‘events’ the duration of which is our primary indicator for trapping. Based on the flow speed alone we expect events due to particles that flow freely through the cavity mode to display durations of about 20 ms, and so we define a trapping event as one with duration exceeding 200 ms preceded by a period exceeding 100 ms with no observed mode shift.

Fig. 3a shows exemplar mode shift events highlighting both trapped and non-trapped particles.

An important consideration for the pressure-driven flow used here is that the flow speed is not uniform but follows a parabolic profile across the flow channel cross section, with zero flow rate at the mirror surfaces. We select the mirror separation such that five anti-nodes of the optical field lie

within the flow channel, whereby we expect about two-thirds of the recorded events to result from the anti-nodes nearest the centre of the flow channel. The parabolic flow profile is included in the simulation to ensure accurate comparison with experimental data.

The distribution  $N(\beta)$  for particles in a solution is measured by sweeping the magnitude of the optical force *via* the laser power while maintaining a constant flow speed. Fig. 3b shows broadly how the number of trap events can be seen to increase with increased laser power.

Fig. 4 and 5 compare experimental (upper row) and simulated (lower row) data for the trapping behaviour as a function of laser power, with each panel comparing two different nanoparticle samples. Sub-figures (a) and (c) show raw data in which the laser power is swept and the rate of trap events is recorded, while sub-figures (b) and (d) show the derivative of these raw data with respect to power which represents a measure of the distribution  $N(\beta)$ .

The experimental data in Fig. 4a and 5a show clear steps in trap rate with laser power, agreeing well with the simulations. The effect of the parabolic flow can be seen by a small increase in trap rate at laser powers below the main step, consistent with the lower threshold of trapping for the slower moving particles close to the mirrors.

Fig. 4a and b show that PS particles of diameter 140 nm and 175 nm are clearly resolved by the technique. The 140 nm particles require about double to power of the 175 nm particles to be trapped, such that the threshold power for trapping scales as  $\sim a^3$  in contrast to eqn (3). This





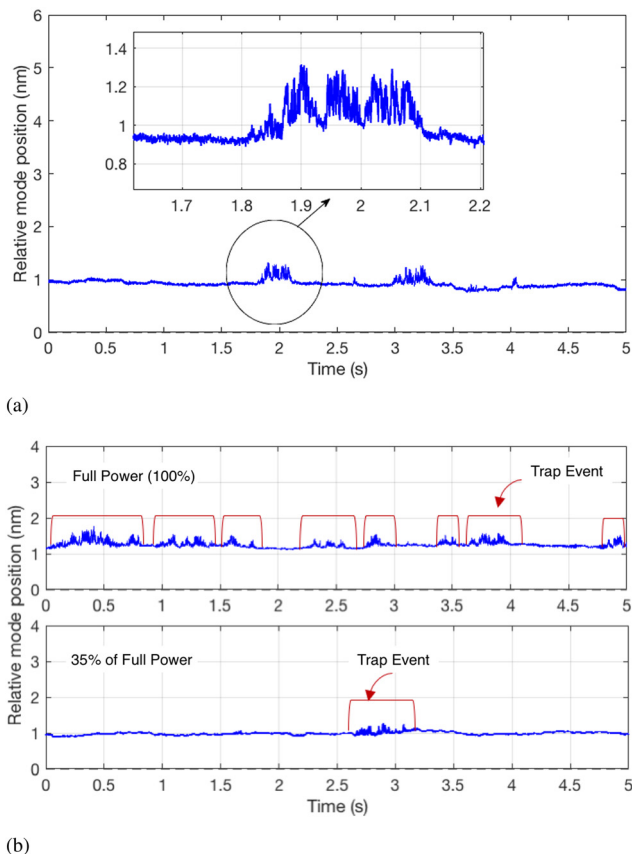


**Fig. 3** Example experimental data showing single particle events. (a) Prolonged mode shift of a trapped particle (b) the effects of laser power on the number of trapping events.

dependency suggests that these experiments are in a regime where the trap time is determined more by the thermal energy than by the fluid flow. The full-width-at-half-maxima of the peaks in Fig. 4b reveals a sizing resolution of about 10 nm. Fig. 5a and b show similarly that PS ( $n_p = 1.59$ ) particles of diameter 187 nm and PMMA ( $n_p = 1.49$ ) particles of size 196 nm are easily distinguished, the PMMA particles requiring a high laser power from trapping despite being slightly smaller. The full-width-at-half-maxima of the peaks in Fig. 5b reveals a refractive index resolution of 0.03 RIU. We note that the resolution of the technique could in principle be increased significantly by increasing both the intracavity power and flow speed. An estimate of the quality factor of the measurement is provided by the optical trap strength: the ratio of the depth of the trap to the thermal energy,

$$Q = \frac{\alpha P}{\pi n c \omega^2 K_B T}. \quad (8)$$

For the experiments presented here,  $Q \sim 3$ , with  $P$  limited to around 20 mW by intracavity heating effects. These occur at a relatively low average power due to the measurement method which sweeps the cavity mode through resonance with the laser, such that the peak power in the cavity is some fifty times greater than the effective  $P$  for trapping.

## 4 Conclusion

While based on single particle measurements, the technique as presented provides only ensemble data in the form of the distribution  $N(\beta)$ . Adaptations could in principle measure  $\beta$

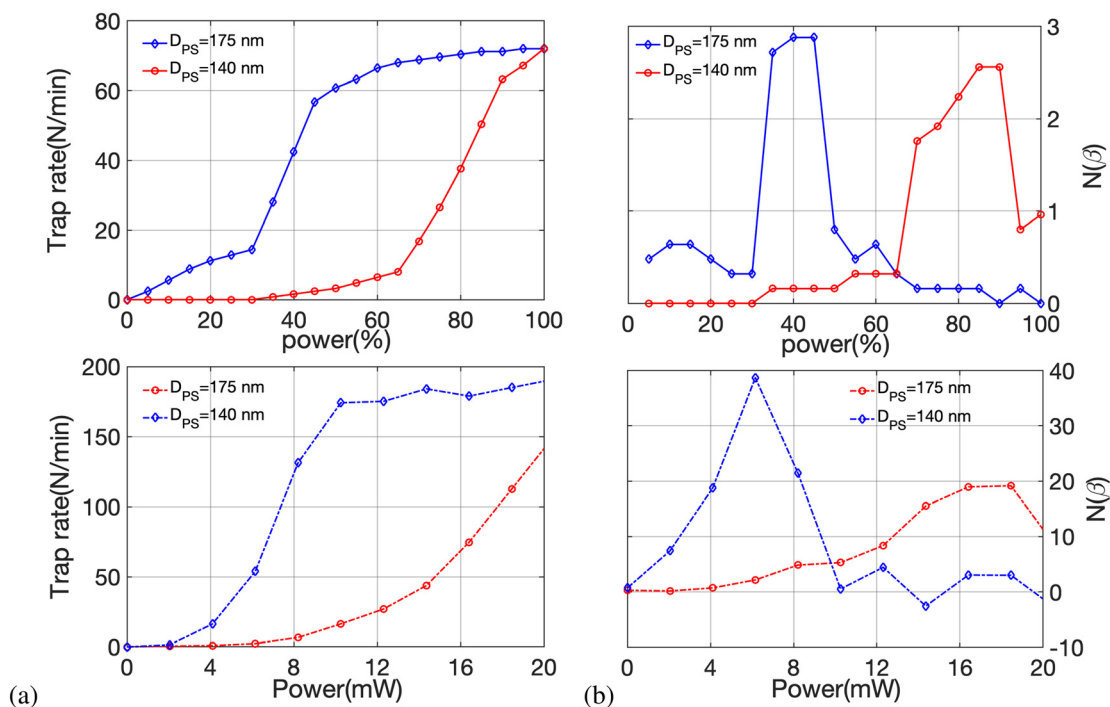


**Fig. 4** Experimental results (upper row) versus simulation results (lower row) when polystyrene (PS) nanoparticles with diameters of 140 nm and 175 nm are introduced through the cavity; (a) trapping rate (left column) and (b) distribution  $N(\beta)$  (right column) against power changes.



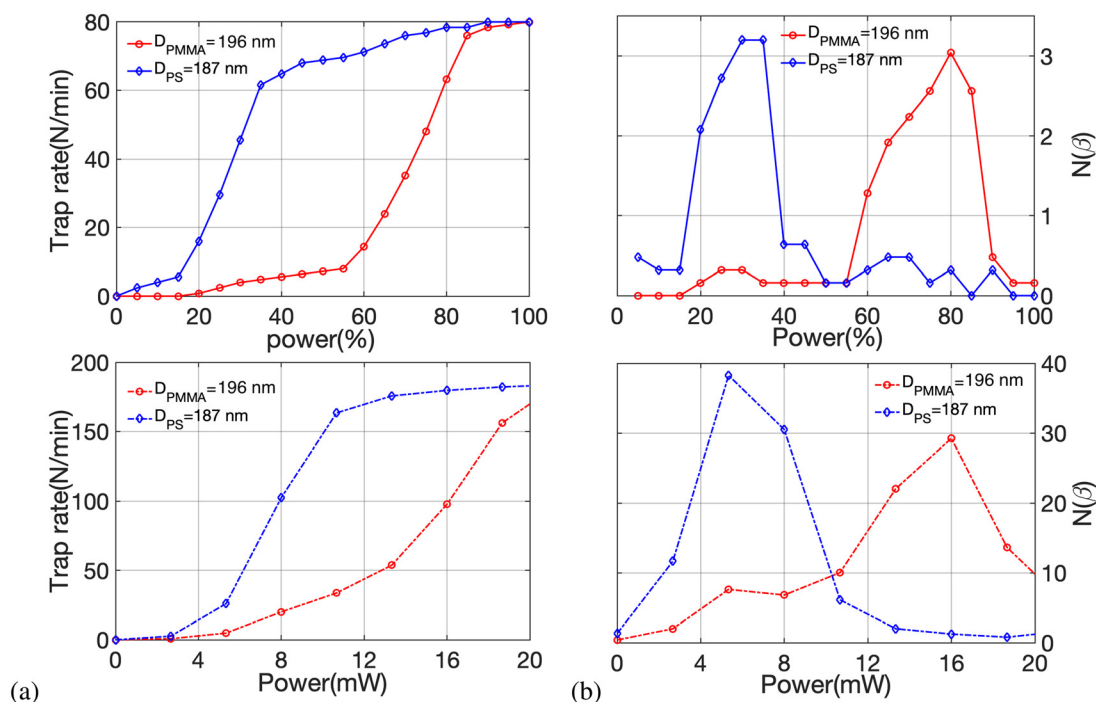


Fig. 5 Experimental results (upper row) versus simulation results (lower row) when 187 nm polystyrene (PS) nanoparticles and 196 nm PMMA nanoparticles are studied; (a) trapping rate (left column) and (b) distribution  $N(\beta)$  (right column) against power changes.

for each particle, potentially by sweeping the trap power during the trapping event. Such developments would be valuable in extending the range of parameters that can be measured on single particles. For example the maximum mode shift provides a measure of the polarizability of each particle<sup>30</sup> and so could be combined with  $\beta$  to yield both particle radius and refractive index.

The measured distribution  $N(\beta)$  provided by this method can be used to establish sample-to-sample variations in

particle size and composition, complementary with other analytic techniques. Since the data recorded contains further information beyond the duration of trap events it is also possible to use this method as part of a wider technique to provide independent measurements of size and composition parameters.

The use of higher average intracavity powers would facilitate higher resolution measurements and measurement of smaller particles. One approach to this would be a configuration in which the trapping laser is 'always on' such that the peak power and average power are equal. Eqn (7) reveals that a factor of 50 increase in  $P$  would lead to a concomitant reduction in  $\beta_T$ , such that particles about seven times smaller would be trapped. Equivalently a larger quality factor  $Q \sim 100$  might be achieved by simultaneously increasing the flow speed to around  $1.5 \text{ mm s}^{-1}$  to provide a resolution to particle size of below 1 nm or to refractive index of order  $10^{-3}$  RIU. An additional benefit of the increased flow speed would be that each trap measurement would take only a few milliseconds to record.

Additional improvements might be achieved by pumping the particles through the cavity using dielectrophoresis, which is capable of establishing a uniform flow rate across the flow channel. The technique might also be used to measure thermophoretic effects that result from particle heating and can provide information on particle thermal conductivity<sup>43,44</sup> or ionic shielding.<sup>45</sup>

As discussed in our previous work,<sup>35</sup> open-access microcavity is a promising method for lab-on-a-chip applications. The proposed technique based on these type of

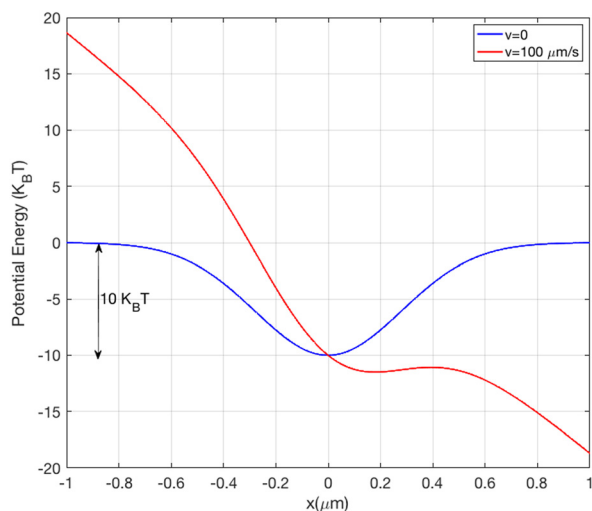


Fig. 6 Total potential energy along the axis ( $x, 0, 0$ ) for a PS particle diameter of 200 nm with no flow (blue curve) and with a flow speed of  $100 \mu\text{m s}^{-1}$  (red curve).



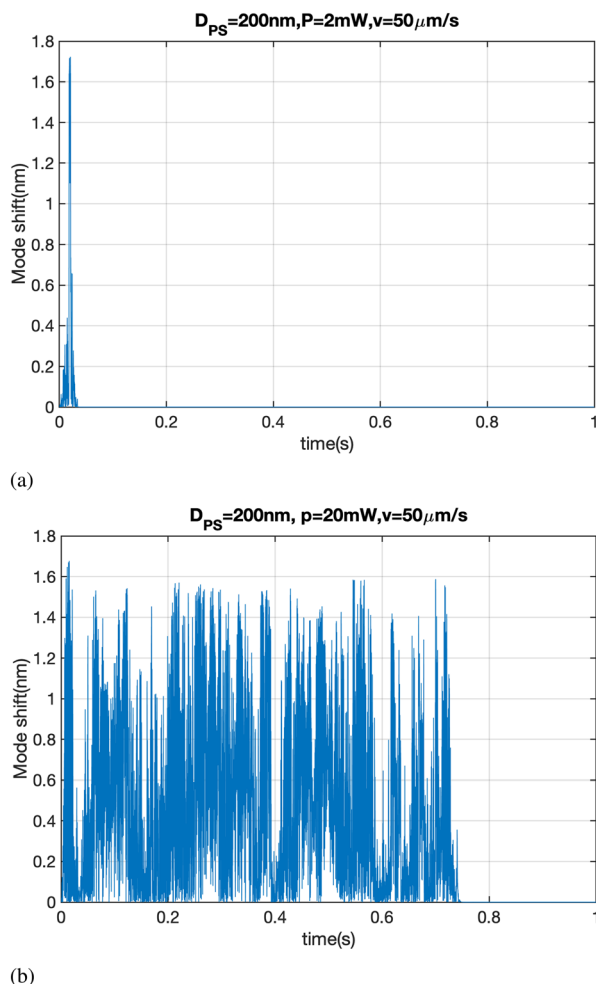


Fig. 7 The mode shift of a PS particle with diameter of 200 nm with a fluid flow speed of  $50 \mu\text{m s}^{-1}$  and intracavity powers of (a) 2 mW and (b) 20 mW.

cavities allows us to effectively evaluate the size distribution of particles in a fluid if particles of known composition are taken with different sizes. Thus, this technique is a promising method to find the range of needed power and flow rate to overcome the Brownian force, and to trap nanoparticles. This result has motivated us to study other methods to increase the average interactivity power, *e.g.*, illuminating the cavity with a light source that provides constant optical injection. Not only this method can measure the size of particles, but also it is sensitive to the refractive index of particles so that we can measure the polarizability of particles as well. The magnitude of the resonance shift reveals the particle polarizability, providing a useful fingerprint that is sensitive to the material composition of the nanoparticle. The technique, therefore, allows the differentiation of particles of similar size, as we showed by the distinction of polystyrene and PMMA particles. Therefore, our method can be used to give a measure of composition such as those used in drug loading for nanomedicine. As a result, this method can be a powerful technique to characterize nanoparticles in a solution in applications where

we need high-resolution measurements at the level of single molecule detection, showing a major breakthrough in nanoparticle characterization.

## A Appendix

### A.1 Gaussian beam parameters

The plano-concave optical microcavity is characterized by the cavity length  $L$  and the radius of curvature of the concave mirror  $R_L$ . The Rayleigh range  $z_R$  of the confined mode is then

$$z_R = L \sqrt{\left(\frac{R_L}{L} - 1\right)}. \quad (\text{A.1})$$

The radius of curvature of the wavefronts  $R(z)$  and the beam radius  $w(z)$  are then given by

$$R(z) = z \left(1 + \left(\frac{z_R}{z}\right)^2\right), \quad (\text{A.2})$$

$$w(z) = \sqrt{\frac{2zR(z)}{kz_R}}. \quad (\text{A.3})$$

The intensity distribution for the resonant cavity mode supported between opposing concave and planar mirrors given in eqn (5) is determined as the sum of two Gaussian beams propagating in opposite directions,  $I = n_m \epsilon_0 c |E_i + E_r|^2$ , where the incident ( $E_i(\rho, z)$ ) and reflected ( $E_r(\rho, z)$ ) waves are given by:<sup>46</sup>

$$E_i(\rho, z) = E_0 \frac{\omega_0}{\omega} \exp\left(\frac{-\rho^2}{\omega^2}\right) \exp\left(ikz + \frac{ik\rho^2}{2R} - i \arctan\left(\frac{z}{z_R}\right)\right), \quad (\text{A.4})$$

$$E_r(\rho, z) = E_0 \frac{\omega_0}{\omega} \exp\left(\frac{-\rho^2}{\omega^2}\right) \exp\left(-ikz - \frac{ik\rho^2}{2R} + i \arctan\left(\frac{z}{z_R}\right)\right). \quad (\text{A.5})$$

### A.2 Balancing optical and flow forces

The maximum optical force is obtained by establishing the maximum value of  $\frac{dI}{dx}$  using the mode intensity in eqn (5). This maximum force opposing the drag force due to the fluid flow occurs at  $x = \frac{w}{2}$ ,  $y = 0$ ,  $z = 0$  at which point  $\frac{dI}{dx} = \frac{2P}{\pi w^3 \sqrt{e}}$ . Substitution of this expression into the optical force term in eqn (1) and equating with the viscous drag force due to fluid flow yields eqn (7). This condition corresponds approximately to the potential energy profile shown in red in Fig. 6, where the potential gradient tends to zero at the downstream side of the cavity mode.



### A.3 Monte Carlo simulation

Based on eqn (1) and (5), and the selection of the  $x$  axis as the flow, the equations for incremental movements of a particle in the Cartesian coordinate system are:

$$x_i = x_{i-1} + \frac{\Delta t}{2n_m \gamma \epsilon_0 c} \alpha \frac{dI(r)}{dx} + \sqrt{\frac{2K_B T \Delta t}{\gamma}} w_i + \Delta t v_{x0}, \quad (\text{A.6})$$

$$y_i = y_{i-1} + \frac{\Delta t}{2n_m \gamma \epsilon_0 c} \alpha \frac{dI(r)}{dy} + \sqrt{\frac{2K_B T \Delta t}{\gamma}} w_i, \quad (\text{A.7})$$

$$z_i = z_{i-1} + \frac{\Delta t}{2n_m \gamma \epsilon_0 c} \alpha \frac{dI(r)}{dz} + \sqrt{\frac{2K_B T \Delta t}{\gamma}} w_i. \quad (\text{A.8})$$

Here  $w_i$  is a computer generated, normally distributed random number with unity variance. The time increment  $\Delta t$  is selected as 1  $\mu\text{s}$  which is short enough to prevent ‘tunneling’ of the particle through the potential barriers. The Monte Carlo model allows simulation of the mode shift with time as the particle moves through the mode  $I(r)$ . Fig. 7a shows example mode shift events of a spherical PS nanoparticle diffusing through the cavity. The diameter and the velocity of the nanoparticle are 200 nm, and 50  $\mu\text{m s}^{-1}$ , respectively. At an intracavity power of 2 mW the particle passes through the cavity mode in about 20 ms while at an intracavity power of 20 mW the particle remains in the mode for about 750 ms (Fig. 7b).

## Conflicts of interest

There are no conflicts to declare.

## Acknowledgements

This work was funded by Oxford HighQ and the University of Oxford.

## Notes and references

- 1 C. A. Barrios, *Anal. Bioanal. Chem.*, 2012, **403**, 1467–1475.
- 2 X. Chen, H. Guan, Z. He, X. Zhou and J. Hu, *Anal. Methods*, 2012, **4**, 1619–1622.
- 3 K. Malmir, H. Habibiyan and H. Ghafoorifard, *Opt. Commun.*, 2016, **365**, 150–156.
- 4 K. Malmir, H. Habibiyan and H. Ghafoorifard, *Optik*, 2020, **216**, 164906.
- 5 N. Malmir and K. Fasihi, *J. Mod. Opt.*, 2017, **64**, 2195–2200.
- 6 F. Caruso, T. Hyeon and V. M. Rotello, *Chem. Soc. Rev.*, 2012, **41**, 2537–2538.
- 7 A. Kamanzi, Y. Gu, R. Tahvildari, Z. Friedenberger, X. Zhu, R. Berti, M. Kurylowicz, D. Witzigmann, J. A. Kulkarni and J. Leung, *et al.*, *ACS Nano*, 2021, **15**, 19244–19255.
- 8 L. M. Payne, W. Albrecht, W. Langbein and P. Borri, *Nanoscale*, 2020, **12**, 16215–16228.
- 9 M. M. Modena, B. Rühle, T. P. Burg and S. Wuttke, *Adv. Mater.*, 2019, **31**, 1901556.
- 10 K.-T. Liao, J. Schumacher, H. J. Lezec and S. M. Stavis, *Lab Chip*, 2018, **18**, 139–152.
- 11 Y. Seo and W. Jhe, *Rep. Prog. Phys.*, 2007, **71**, 016101.
- 12 J. Stetefeld, S. A. McKenna and T. R. Patel, *Biophys. Rev.*, 2016, **8**, 409–427.
- 13 S. Soares, J. Sousa, A. Pais and C. Vitorino, *Front. Chem.*, 2018, **6**, 360.
- 14 S. Mourdikoudis, R. M. Pallares and N. T. Thanh, *Nanoscale*, 2018, **10**, 12871–12934.
- 15 A. Surrey, D. Pohl, L. Schultz and B. Rellinghaus, *Nano Lett.*, 2012, **12**, 6071–6077.
- 16 E. Orlova and H. R. Saibil, *Chem. Rev.*, 2011, **111**, 7710–7748.
- 17 E. Nakamura, N. A. Sommerdijk and H. Zheng, *Acc. Chem. Res.*, 2017, **50**, 1795–1796.
- 18 V. Filipe, A. Hawe and W. Jiskoot, *Pharm. Res.*, 2010, **27**, 796–810.
- 19 C. Troiber, J. C. Kasper, S. Milani, M. Scheible, I. Martin, F. Schaubhut, S. Kuchler, J. Rädler, F. C. Simmel and W. Friess, *et al.*, *Eur. J. Pharm. Biopharm.*, 2013, **84**, 255–264.
- 20 N. C. Bell, C. Minelli and A. G. Shard, *Anal. Methods*, 2013, **5**, 4591–4601.
- 21 C. Haiden, T. Wopelka, M. Jech, F. Keplinger and M. J. Vellekoop, *Langmuir*, 2014, **30**, 9607–9615.
- 22 S. Block, B. J. Fast, A. Lundgren, V. P. Zhdanov and F. Höök, *Nat. Commun.*, 2016, **7**, 1–8.
- 23 P. C. Simons, S. M. Young, M. B. Carter, A. Waller, D. Zhai, J. C. Reed, B. S. Edwards and L. A. Sklar, *Nat. Protoc.*, 2011, **6**, 943–952.
- 24 G. Grégori, V. Patsekin, B. Rajwa, J. Jones, K. Ragheb, C. Holdman and J. P. Robinson, *Cytometry, Part A*, 2012, **81**, 35–44.
- 25 S. Zhu, L. Ma, S. Wang, C. Chen, W. Zhang, L. Yang, W. Hang, J. P. Nolan, L. Wu and X. Yan, *ACS Nano*, 2014, **8**, 10998–11006.
- 26 A. G. Shard, K. Sparnacci, A. Sikora, L. Wright, D. Bartczak, H. Goenaga-Infante and C. Minelli, *Anal. Methods*, 2018, **10**, 2647–2657.
- 27 C. Minelli, A. Sikora, R. Garcia-Diez, K. Sparnacci, C. Gollwitzer, M. Krumrey and A. G. Shard, *Anal. Methods*, 2018, **10**, 1725–1732.
- 28 G. Young, N. Hundt, D. Cole and P. Kukurra, *Science*, 2018, **360**, 423–427.
- 29 N. Mojarad and M. Krishnan, *Nat. Nanotechnol.*, 2012, **7**, 448–452.
- 30 A. Trichet, P. Dolan, D. James, G. Hughes, C. Vallance and J. Smith, *Nano Lett.*, 2016, **16**, 6172–6177.
- 31 <https://www.oxfordhighq.com>.
- 32 K. Ladavac, K. Kasza and D. G. Grier, *Phys. Rev. E: Stat., Nonlinear, Soft Matter Phys.*, 2004, **70**, 010901.
- 33 M. P. MacDonald, G. C. Spalding and K. Dholakia, *Nature*, 2003, **426**, 421–424.
- 34 P. T. Korda, M. B. Taylor and D. G. Grier, *Phys. Rev. Lett.*, 2002, **89**, 128301.
- 35 A. Trichet, J. Foster, N. Otori, D. James, P. Dolan, G. Hughes, C. Vallance and J. Smith, *Lab Chip*, 2014, **14**, 4244–4249.





- 36 G. Volpe and G. Volpe, *Am. J. Phys.*, 2013, **81**, 224–230.
- 37 L. Giriunas, *et al.*, *J. Appl. Phys.*, 2018, **124**, 025703.
- 38 Z. Geng, *et al.*, *Phys. Rev. Lett.*, 2020, **124**, 153603.
- 39 Z. Geng, K. Peters, A. Trichet, K. Malmir, R. Kolkowski, J. Smith and S. Rodriguez, 2019, preprint arXiv:1911.00463, DOI: [10.48550/arXiv.1911.00463](https://doi.org/10.48550/arXiv.1911.00463).
- 40 K. Peters, Z. Geng, K. Malmir, J. Smith and S. Rodriguez, 2020, preprint arXiv:2008.11615, DOI: [10.48550/arXiv.1911.00463](https://doi.org/10.48550/arXiv.1911.00463).
- 41 K. Peters, *et al.*, *Phys. Rev. Lett.*, 2021, **126**, 213901.
- 42 Datasheet, *OB1–4 channels microfluidic flow controller*.
- 43 G. McNab and A. Meisen, *J. Colloid Interface Sci.*, 1973, **44**, 339–346.
- 44 R. T. Schermer, *et al.*, *Opt. Express*, 2011, **19**, 10571–10586.
- 45 S. Duhr and D. Braun, *Proc. Natl. Acad. Sci. U. S. A.*, 2006, **103**, 19678–19682.
- 46 P. Zemánek, A. Jonáš, L. Šrámek and M. Liška, *Opt. Commun.*, 1998, **151**, 273–285.

